Supporting Information

Space-Confined Mediation of Electron Transfer for Efficient Biomolecular Solar Conversion

Margot Jacquet, Miriam Izzo, Piotr Wróbel, Marcin Strawski, Massimo Trotta, Rafał Jurczakowski and Joanna Kargul**

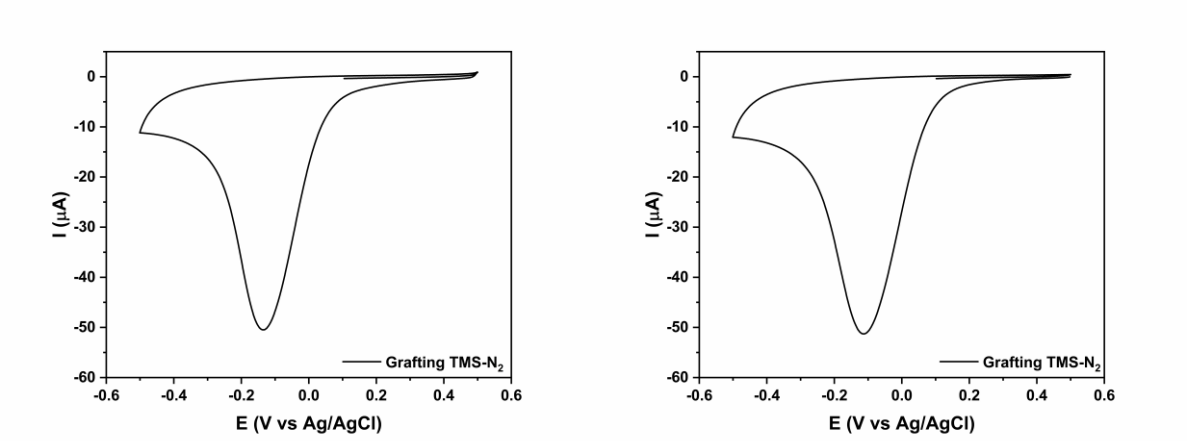

Fig. S1. Representative cyclic voltammograms recorded during the electrografting of TMS-N_2 in 0.1 M acetonitrile/ NBu_4PF_6 electrolyte, at 50 mV s^{-1}.

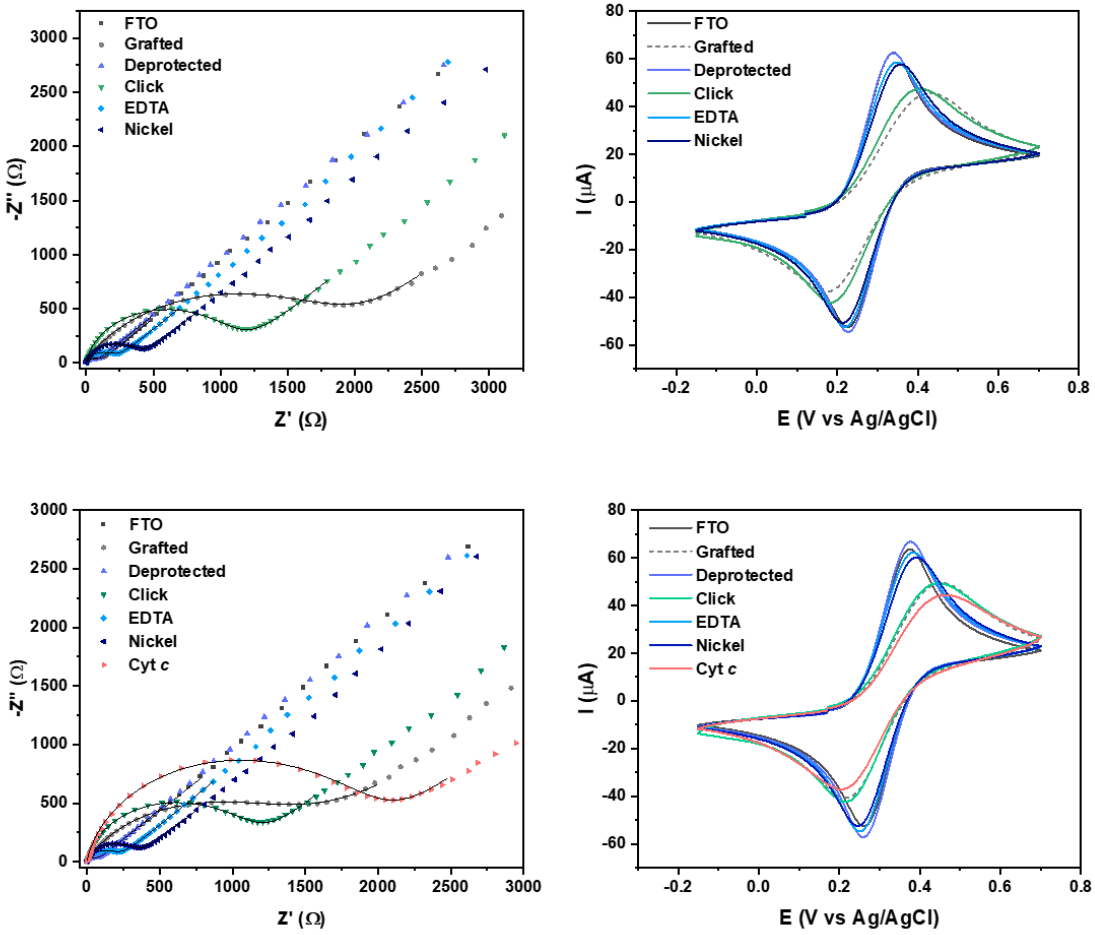

Fig. S2. Nyquist plot with fitted curves of electrochemical impedance spectra (left) and corresponding cyclic voltammetry at 100 mV s^{-1} (right) obtained for FTO-*c*NTA-Ni (top) and FTO-*c*NTA-Ni-cyt (bottom) electrodes at different steps of functionalization. All measurements were performed with 1 mM 1,1'-ferrocenedimethanol in 0.1 M phosphate buffer (PB, pH 7).

Table S1. The curve fitting results based on $R_S((R_{CT}W)CPE)$ model and calculated capacitance C_{dl} for FTO electrodes at each step of functionalization with 1 mM 1,1'-ferrocenedimethanol in 0.1 M PB (pH 7)

	FTO-cNTA-Ni					FTO-cNTA-Ni-cyt					FTO-cNTA-Ni-cyt-PSI				
	R_S ($\Omega \cdot cm^2$)	R_{CT} ($\Omega \cdot cm^2$)	C_{dl} ($\mu F/cm^2$)	Q (10^{-6})	Φ	R_S ($\Omega \cdot cm^2$)	R_{CT} ($\Omega \cdot cm^2$)	C_{dl} ($\mu F/cm^2$)	Q (10^{-6})	Φ	R_S ($\Omega \cdot cm^2$)	R_{CT} ($\Omega \cdot cm^2$)	C_{dl} ($\mu F/cm^2$)	Q (10^{-6})	Φ
FTO	103.3	36.5	6.3	8.5	0.85	110.4	27.7	7.3	9.9	0.85	122.3	35.9	8.4	11.5	0.84
Grafted	114.5	786.9	19.0	28.2	0.68	112.7	551.4	18.8	28.5	0.7	110.1	748.1	17.0	23.3	0.71
Deprotected	107.7	26.9	10.0	3.8	0.86	112.5	26.9	10.4	14.1	0.85	112.2	29.9	12.0	17.5	0.83
Click	155.2	420.6	11.7	7.6	0.90	141.4	432.9	12.6	8.2	0.90	113.5	330.6	12.5	9.4	0.88
EDTA	113.6	79.7	11.8	9.6	0.89	113.6	79.0	12.4	10.7	0.88	114.5	101.8	13.3	11.7	0.88
Nickel	110.8	149.9	11.1	8.8	0.89	112.3	128.8	11.9	9.6	0.89	114.3	190.0	12.3	9.7	0.88
Cyt *c*	-	-	-	-	-	132.8	748.8	16.3	9.9	0.90	120.4	843.1	17.0	10.5	0.89
PSI	-	-	-	-	-	-	-	-	-	-	132.8	1474.9	15.8	9.0	0.90

Supporting text to Fig. S2 and Table S1. The charge transfer resistance R_{CT} and the double-layer capacitance C_{dl} (calculated from CPE parameters Q and Φ)[1] of the pristine and functionalized electrodes were obtained by fitting the EIS data with the equivalent circuit model $R_S((R_{CT}W)CPE)$, where R_S corresponds to the electrolyte resistance, R_{CT} represents the charge transfer resistance between the analysed electrode and the electrolyte, W stands for the Warburg impedance induced by the diffusion process, and CPE is the constant-phase element of the double-layer capacitance existing between the solid/liquid phases.

The recorded evolution of the R_{CT} and C_{dl} until the metalation step is fully in line with our previously described results.[2] After the electrografting of the protected alkyne behaving as an insulator layer, the R_{CT} value increased drastically, followed by a decrease of the R_{CT} value close to the pristine FTO R_{CT} value after the deprotection step, typical for a conductive thin monolayer or submonolayer. The formation of the triazole bridge by the click chemistry reaction is accompanied by an increase of the R_{CT} which is later decreased after the addition of EDTA to remove any residual chelated copper ions involved during the click reaction. Finally, after the metalation step, a slight increase of the R_{CT} value is obtained possibly explained by electrostatic interactions between the positively charged metal ion and the negatively charged FTO, resulting in a dense monolayer diminishing the access of the redox probe to the surface. As described in the manuscript, the immobilization of the proteins (cyt *c* and PSI) results in a consequent increase of the R_{CT} values attributed to their compact protein backbone hindering the access of Fc to the electrode surface. Concerning the capacitance C_{dl}, the stable tendency observed after the deprotection step until the protein immobilization supported by an exponential factor Φ closed to unity ($0.83 < \Phi < 0.90$) testify to a homogeneous and well-architectured interface, whilst the increased C_{dl} values obtained with cyt *c* and PSI are explained by the presence of partial charges existing in the protein backbone.

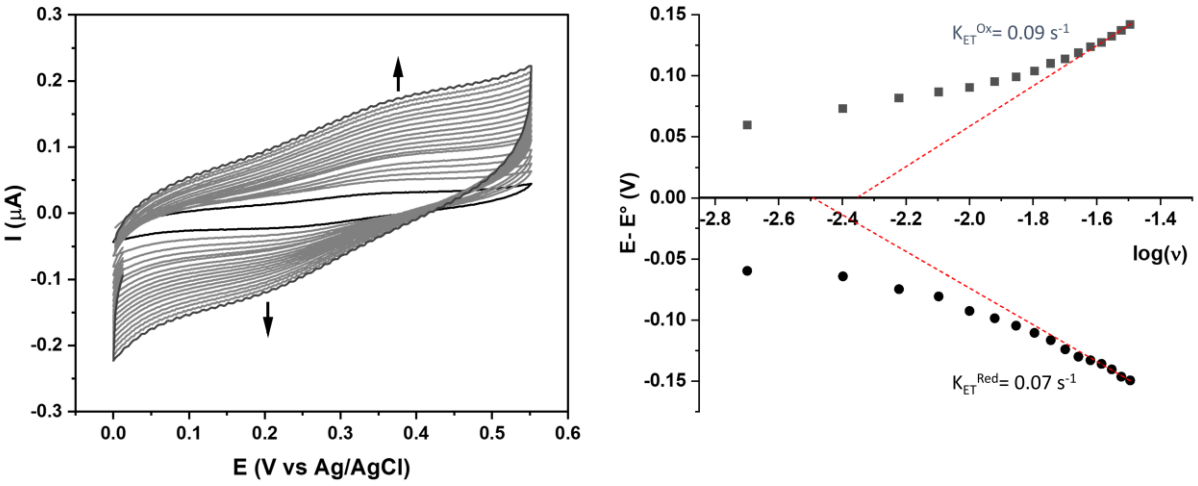

Fig. S3. Cyclic voltammograms of FTO-*c*NTA-Ni-cyt at various scan rates from 2 $mV.s^{-1}$ to 38 $mV.s^{-1}$ in 5 mM PB solution (pH 7). Corresponding Laviron's plot for the determination of the interfacial electron transfer kinetics (k_{ET}).

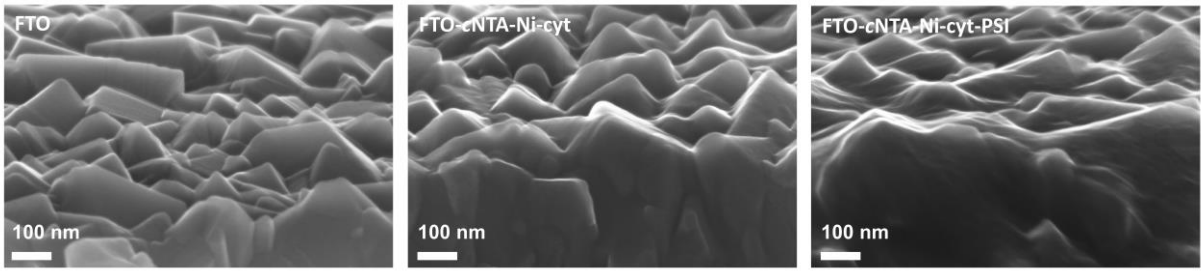

Fig. S4. Scanning Electron Microscopy images of the bare FTO, and biohybrid configurations FTO-*c*NTA-Ni-cyt and FTO-*c*NTA-Ni-cyt-PSI, recorded at 75° with a 300.00 KX magnification (EHT = 15.00 kV).

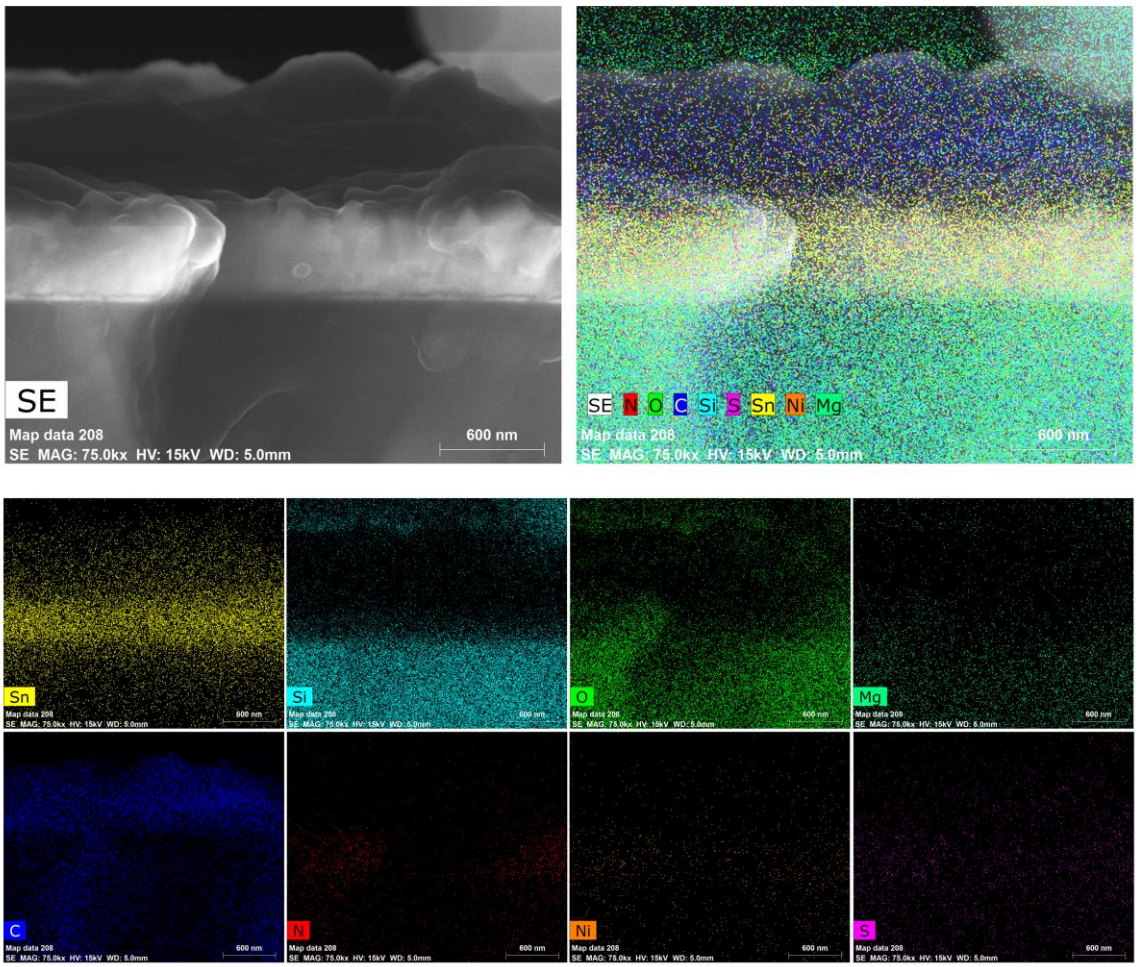

Fig. S5. Scanning Electron Microscopy (SEM) images coupled to Energy Dispersive Spectroscopy (EDS) elemental mapping of the biohybrid configuration FTO-*c*NTA-Ni-cyt-PSI, recorded at 90° using a 75.00 KX magnification (EHT = 15.00 kV).

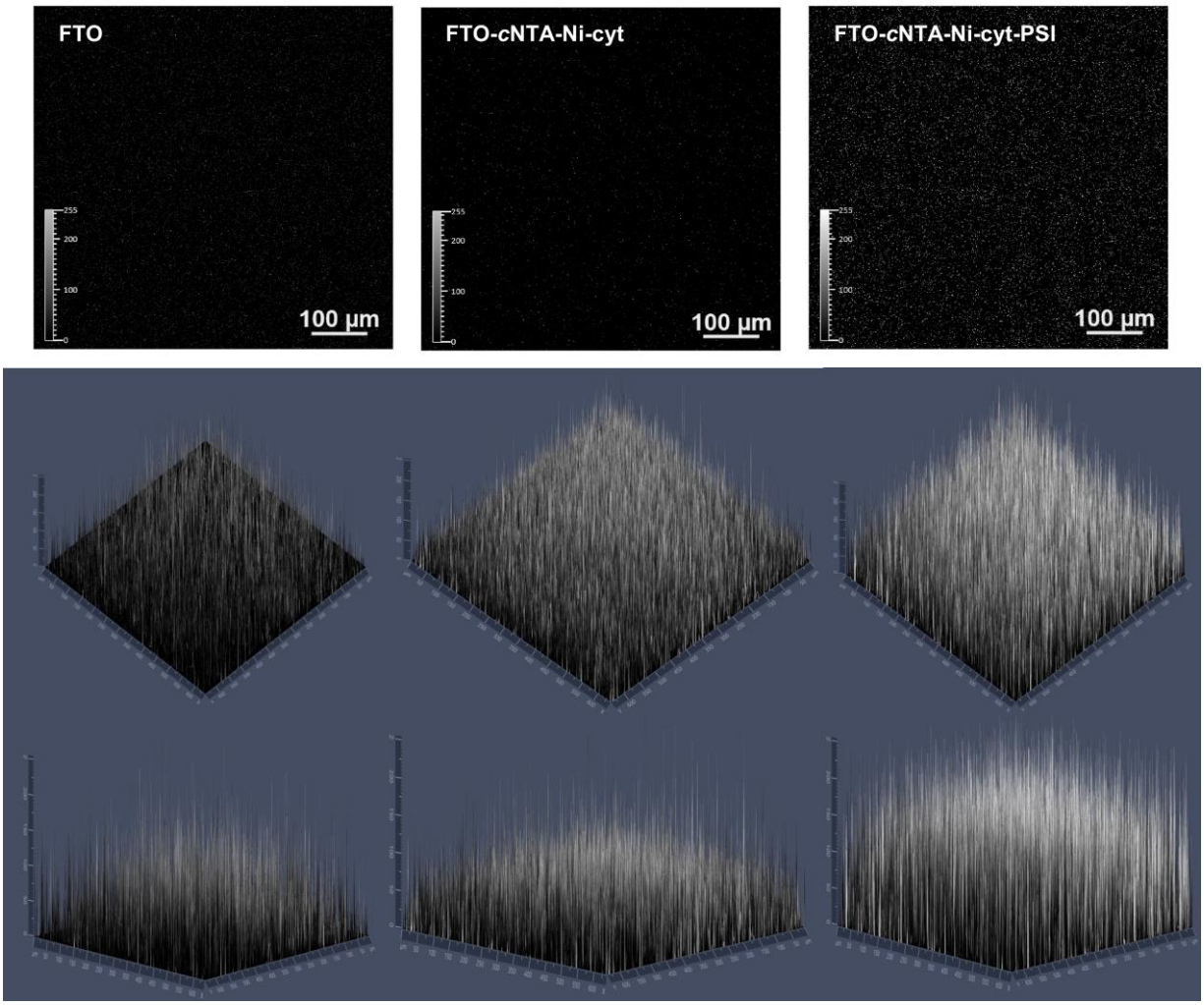

Fig. S6. Confocal fluorescence imaging of the FTO (left), FTO-*c*NTA-Ni-cyt (middle) and FTO-*c*NTA-Ni-cyt-PSI (right) electrodes, 2D (top) and 2.5D (bottom) fluorescence intensity maps. The visualized area is ~ 0.63 mm^2. Excitation at 639 nm. Fluorescence distribution is represented with a height map using an intensity range from 0 to 255.

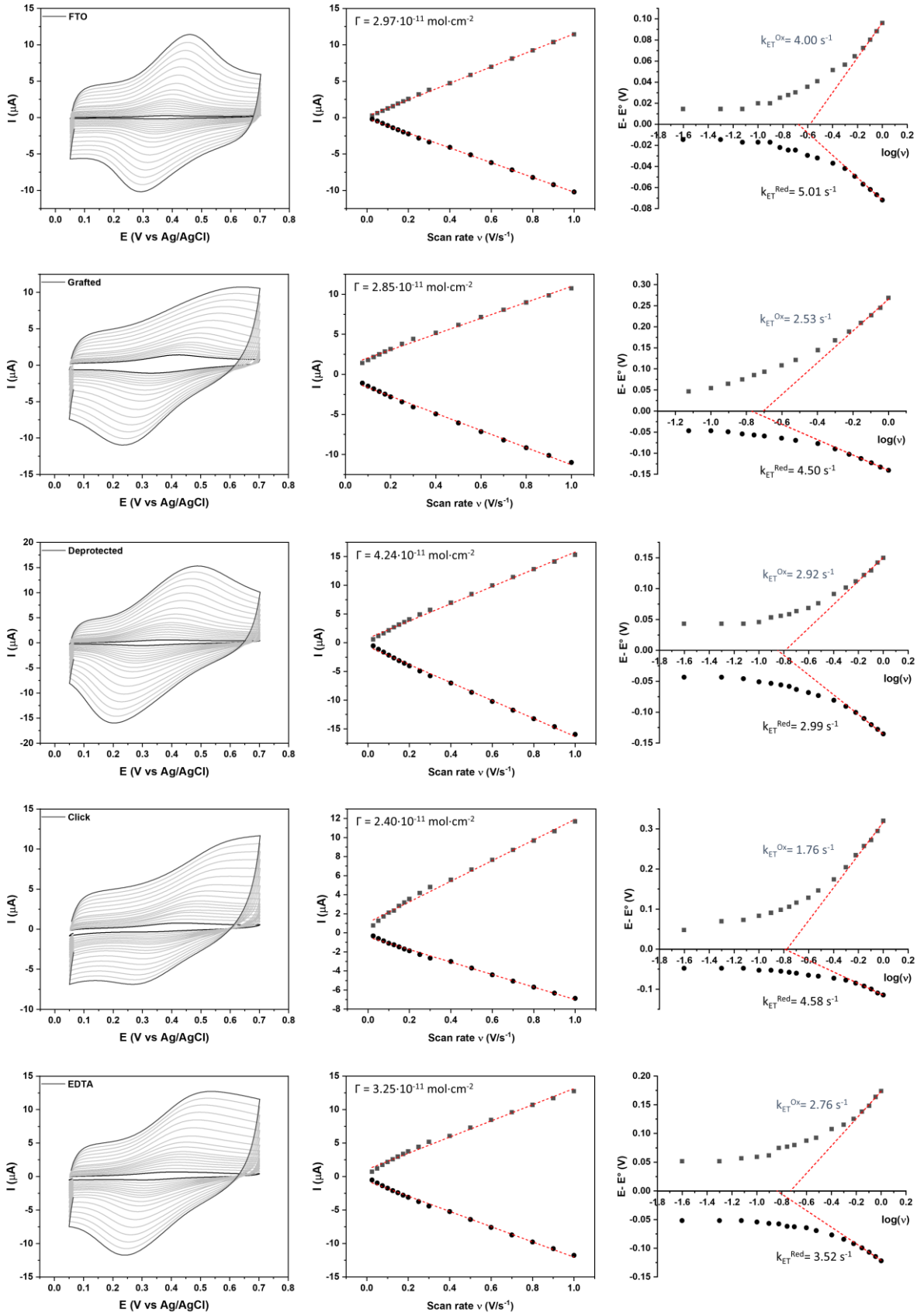
FTO
Γ = 2.97·10-11 mol·cm-2
kET Ox= 4.00 s-1
kET Red= 5.01 s-1
Grafted
Γ = 2.85·10-11 mol·cm-2
kET Ox= 2.53 s-1
kET Red= 4.50 s-1
Deprotected
Γ = 4.24·10-11 mol·cm-2
kET Ox= 2.92 s-1
kET Red= 2.99 s-1
Click
Γ = 2.40·10-11 mol·cm-2
kET Ox= 1.76 s-1
kET Red= 4.58 s-1
EDTA
Γ = 3.25·10-11 mol·cm-2
kET Ox= 2.76 s-1
kET Red= 3.52 s-1
I (µA)
E (V vs Ag/AgCl)
Scan rate ν (V/s-1)
E- E° (V)
log(ν)

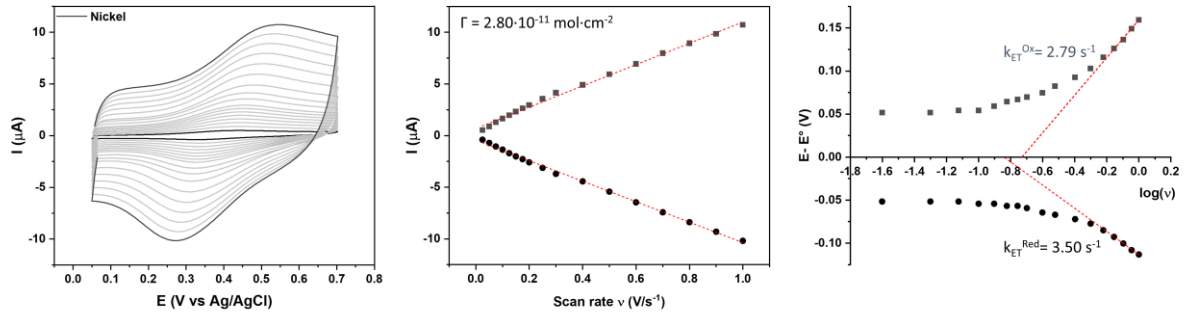

Fig. S7. Electrochemical investigation of the Fc entrapment at each step of the functionalization: FTO / Grafted / Deprotected / Click / EDTA / Nickel. (left) Cyclic voltammograms at various scan rates from 0.025 V.s^{-1} to 1 V.s^{-1} in 5 mM PB. (middle) Linear dependency of the current (*I*) vs. the scan rate (υ) with the calculated surface coverage *Γ*. (right) Corresponding Laviron's plot for the determination of the interfacial electron transfer kinetics k_{ET}.

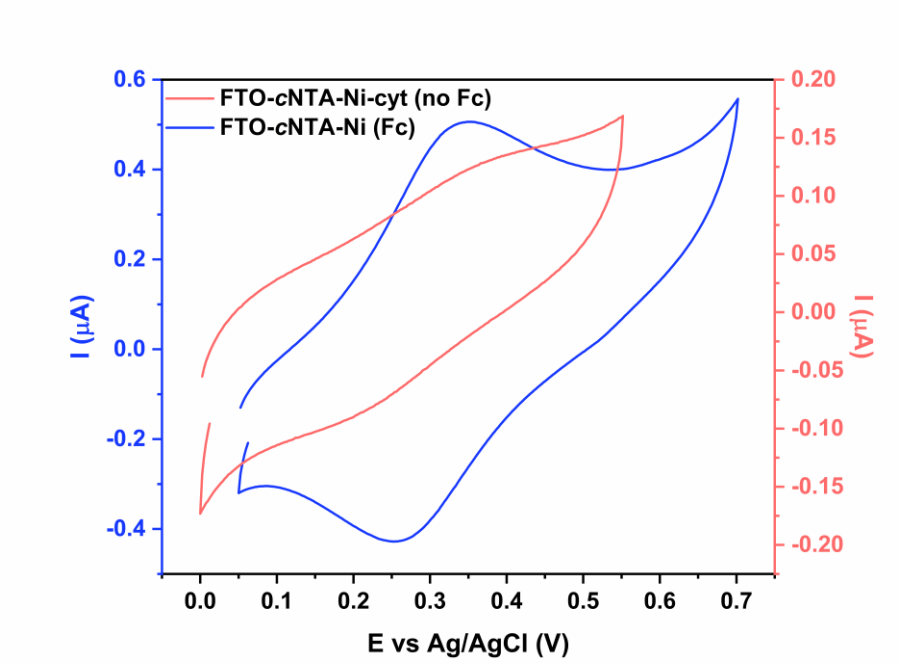

Fig. S8. Cyclic voltammograms of FTO-*c*TA-Ni (with entrapped Fc) and FTO-*c*NTA-Ni-cyt (without entrapped Fc) recorded at 25 and 26 mV s^{-1} respectively, in deoxygenated 5 mM PB solution.

Table S2. Photocurrent density J_{photo} obtained during chopped light irradiation (30s. ON/OFF cycles) for functionalized FTO electrodes at different applied potentials vs. Ag/AgCl in aerated 5 mM PB (pH 7). Values reported in the table were obtained from the average of 5 consecutive cycles with two independent replicas.

	Photocurrent density J_{photo} (nA/cm^2)							
	−300 mV	−200 mV	−100 mV	0 mV	100 mV	200 mV	300 mV	400 mV
FTO-cNTA-Ni (Fc)	−651 ± 3	−266 ± 2	−142 ± 8	−76 ± 2	−37 ± 4	18 ± 2	38 ± 6	70 ± 16
FTO-cNTA-Ni (no Fc)	−531 ± 63	−285 ± 32	−147 ± 19	−38 ± 6	14 ± 1	40 ± 1	43 ± 1	56 ± 1
FTO-cNTA-Ni-cyt (Fc)	−834 ± 48	−305 ± 53	−137 ± 45	−81 ± 29	−47 ± 20	0 ± 14	26 ± 2	60 ± 6
FTO-cNTA-Ni-cyt (no Fc)	−592 ± 17	−227 ± 56	−113 ± 17	−60 ± 12	−25 ± 9	13 ± 4	31 ± 4	46 ± 5
FTO-cNTA-Ni-cyt-PSI (Fc)	−934 ± 8	−152 ± 24	−71 ± 9	−38 ± 4	−13 ± 2	18 ± 5	24 ± 8	38 ± 13
FTO-cNTA-Ni-cyt-PSI no (Fc)	−371 ± 3	−71 ± 17	−23 ± 18	−7 ± 9	3 ± 2	12 ± 5	17 ± 8	21 ± 11

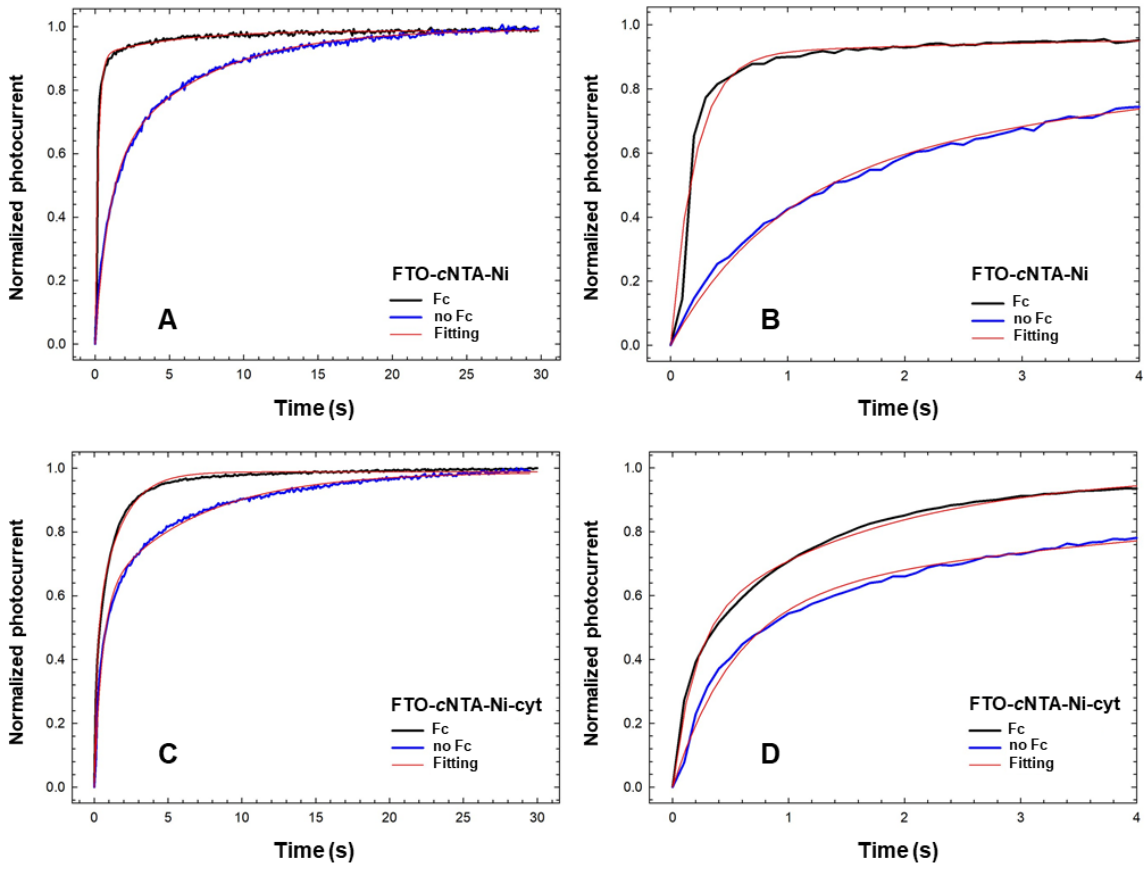

Fig. S9. Normalized photocurrent as function of time obtained at 0 mV vs Ag/AgCl in aerated 5 mM PB for the samples FTO-*c*NTA-Ni (top) and FTO-*c*NTA-Ni-cyt (bottom) with and without entrapped Fc. The data were fit with a biexponential rise to maximum $I = a \times (1\text{-}\exp(\text{-}k_1 t)) + c \times (1\text{-}\exp(\text{-}k_2 t))$. Panels B and D are enlargements of panels A and C, respectively. See supporting text for details.

Table S3. Parameters obtained by fitting the normalized photocurrents in Fig. S8 with a biexponential raise the maximum function $I = a \times (1\text{-}\exp(-k_1 t)) + c \times (1\text{-}\exp(-k_2 t))$.

Fitting parameters	FTO-*c*NTA-Ni		FTO-*c*NTA-Ni-cyt	
	Fc	no Fc	Fc	no Fc
a	0.91±0.01	0.53±0.01	0.48±0.01	0.59±0.01
k_1 (s^{-1})	4.8±0.1	1.12±0.01	5.6±0.2	1.86±0.04
c	0.08±0.01	0.46±0.01	0.51±0.01	0.40±0.01
k_2 (s^{-1})	0.19±0.01	0.156±0.003	0.611±0.01	0.153±0.003
R square	0.9668	0.9978	0.9935	0.9959

Supporting text to Fig. S9 and Table S3.

The presence of Fc within either the FTO-*c*NTA-Ni or FTO-*c*NTA-Ni-cyt architectures accelerates the rise of the photocurrent, as shown from the recorded photocurrent profiles. To quantify the improvement factor, a fitting analysis was performed on the normalized photocurrents as a function of time (shown in Fig. S8) with a biexponential rise to maximum $I = a \times (1\text{-}\exp(-k_1 t)) + c \times (1\text{-}\exp(-k_2 t))$, where I is the normalized photocurrent, t is the time in seconds and the coefficients a and c represent the contribution of each phase, while k_1 and k_2 represent the rates of the two-exponential raising.

The rise of the normalized photocurrent for the abiotic (FTO-*c*NTA-Ni) and biotic (FTO-*c*NTA-Ni-cyt) systems adopts a biexponential behaviour, irrespectively of the presence or absence of Fc, with the fast (k_1) and slow (k_2) components with the corresponding coefficients a and c representing the contribution of each kinetic phase. The fitting data are summarized in Table S3.

Whilst the exact nature of the two exponential contributions remains to be further elucidated, a clear improvement of the photocurrent kinetics by the presence of space-confined Fc is evidenced for both abiotic and biotic configurations with faster exponential rates k_1 and k_2. In the case of FTO-*c*NTA-Ni system, an improvement factor of 4.3 is achieved for k_1 (4.8 s^{-1} *vs* 1.12 s^{-1}) and 1.2 for k_2 (0.19 s^{-1} *vs* 0.156 s^{-1}). For the cyt-based biohybrid FTO-*c*NTA-Ni-cyt system, these improvement factors are 3.0 and 4.0 for k_1 (5.6 s^{-1} *vs* 1.86 s^{-1}) and k_2 (0.611 s^{-1} *vs* 0.153 s^{-1}), respectively. Interestingly, in both systems devoid of entrapped Fc, the contributions of the two exponential components (a and c) remain nearly unchanged, with slightly faster exponential rates for the biohybrid system. However, in the case of the systems with space-confined Fc, a significant difference is visible for the two exponential contributions, indicating that Fc beneficially influences various electron transfer (ET) processes occurring within the biohybrid architecture, which ultimately results in the faster photo-induced ET compared to the Fc-free system.

To rationalize the extrapolated fitting parameters and to obtain a clear and simplified picture of the effect of Fc on the photo-induced ET kinetics in the different architectures, an apparent photocurrent kinetics rate (k_{app}) can be estimated by adding the different exponential rates (k_1 and k_2) multiplied by their respective contribution coefficient (a and c), such as $k_{app} = a \times k_1 + c \times k_2$.

	FTO-*c*NTA-Ni		FTO-*c*NTA-Ni-cyt	
	Fc	no Fc	Fc	no Fc
k_{app} (s^{-1})	4.38	0.67	3.00	1.16

The k_{app} values obtained from the kinetic curves in Fig. S8 clearly indicate the enhancement of the photo-induced ET rate associated with the Fc entrapped within the abiotic and biotic architectures.

Table S4. Current densities obtained during prolonged dark (J_{dark}) and illumination conditions (J_{light}) and the corresponding overall photocurrent density (J_{photo}) for functionalized FTO electrodes at -300 mV vs. Ag/AgCl in aerated 5 mM PB electrolyte (pH 7).

	Current density *J* recorded at −300 mV vs Ag/AgCl		
	J_{irr} (µA/cm²)	J_{dark} (µA/cm²)	J_{photo} (µA/cm²)
FTO-*c*NTA-Ni (Fc)	−7.09	−4.42	−2.67
FTO-*c*NTA-Ni (no Fc)	−2.52	−1.54	−0.98
FTO-*c*NTA-Ni-cyt (Fc)	−11.15	−6.96	−4.19
FTO-*c*NTA-Ni-cyt (no Fc)	−1.64	−0.97	−0.67
FTO-*c*NTA-Ni-cyt-PSI (Fc)	−30.87	−16.84	−14.03
FTO-*c*NTA-Ni-cyt-PSI (no Fc)	−12.74	−7.36	−5.38

Table S5. Maximum photocurrent density J_{photo} of planar (2D) and nanostructured (3D) PSI-based biophotocathode

System	Biocatalyst(s)	Conditions	Diffusive mediators	J_{photo} (µA/cm²)	References
		Planar electrode (2D)			
Planar ITO /PSI	PSI from *Arabidopsis thaliana*	100mW/cm² AM 1.5 solar simulator, 5mM PB , E = -0.3V vs Ag/AgCl	5mM DCPIP + 100mM AscH + 100mM NaCl	-0.7	Adv. Funct. Mater., 2016, 26, 6682
Planar FTO / SIF/ SLG /pyr-NTA-Co/ cyt c / PSI	PSI from *C. merolae* Cyt *c* his_6-tagged genetically engineered from *E. coli.*	100mW/cm² white light, 5mM PB (pH 7), E = -0.3V vs Ag/AgCl	none	-1.5	J. Mater. Chem. C, 2020, 8, 5807
Planar ITO / SAM / AgND / PSI	PSI from *T. elongatus*	25mW/cm² LED 565nm, E = OCP	2 mM MV^{2+} (aq.)	-0.2	ACS Appl. Nano Mater. 2021, 4, 1209
Planar gold / P-Os / PSI	PSI from *T. elongatus*	51mV/cm² He-Xe lamp with red filter >600nm, 150 mM phosphate-citrate buffer (pH 4), E = 0.01V vs Ag/AgCl	2 mM MV^{2+}	-9	Angew. Chem. Int. Ed., 2021, 60, 2000
Planar ITO / p-C_3N_4 / PSI	PSI from spinach *S. oleracea*	100mW/cm² Xe-lamp solar simulator, 20 mM MES buffer, E = -0.2V vs Ag/AgCl	62uM DCPIP + 40 mM AscH	-0.22	ACS Appl. Nano Mater. 2023, 6, 9453
Planar gold / SAM/ PEDOT:PSS / PSI	PSI from spinach	100mW/cm² cold white light, 100mM KCl, E = OCP (0.2V vs Ag/AgCl)	100uM $K_4[Fe(CN)_6]$. $3H_2O$ + 100uM $K_3[Fe(CN)_6]$	-0.7	ACS Appl. Polym. Mater. 2023, 5, 3278

Planar gold / PSI / PPy	PSI from spinach	140 mW/cm^2 cold white light source, 0.1M KCl, E = OCP	1mM DCPIP + 20 mM AscH	-0.49	Nanoscale Adv., 2023, 5, 5301
Planar gold / PSI	PSI from spinach	80mW/cm^2 cold light source, 1M KCl, E = OCP (-0.06V vs Ag/AgCl)	1mM DCPIP + 20 mM AscH	-0.14	ACS Appl. Polym. Mater. 2022, 4, 7852
Planar gold /PPA-PSI	PSI from baby spinach leaves	100mW/cm^2 cold white light, 100mM KCl, E = OCP	1.0 mM $K_4[Fe(CN)_6].3H_2O$ + 1.0 mM $K_3[Fe(CN)_6]$	-6	Nanoscale Adv., 2024, 6, 620
Planar FTO / cNTA-Ni / cyt c/ PSI (Fc-confined)	PSI from *C. merolae* Cyt *c* his_6-tagged genetically engineered from *E. coli.*	100mW/cm^2 white light, 5mM PB (pH 7), E = -0.3V vs Ag/AgCl	none	-14.03	**This work**
Planar FTO / cNTA-Ni / cyt c/ PSI (Fc-free)	-	-	none	-5.38	**This work**
Nanostructured electrode (3D)					
Macroporous ATO / PSI	PSI from *Arabidopsis thaliana*	100mW/cm^2 AM 1.5 solar simulator, 5mM PB , E = -0.3V vs Ag/AgCl	5mM DCPIP + 100mM AscH + 100mM NaCl	-7.7	Adv. Funct. Mater., 2016, 26, 6682
Porous ATO / PSI	PSI from *T. elongatus*	Halogen lamp 310mW, 5mM PB, E = -0.2V vs Ag/AgCl	none	-1.5	ACS Appl. Electron. Mater., 2021, 3, 2087
Porous ATO / cyt c / PSI	PSI from *T. elongatus* Cyt *c* from horse heart	-	none	-4	-
FTO/ Mesoporous NiO / PSI	PSI from *T. vulcanus*	85mW/cm^2 Xe lamp with AM 1.5G solar simulator, 0.1M PB + 0.1M $NaClO_4$, E = 0V vs Ag/AgCl	3 mM MV^{2+}	-1.1	RSC Adv., 2020, 10, 15734
-	-	-	none	-0.75	-
3D rGO / cyt c /PSI	PSI from *T. elengatus* Cyt *c* from horse heart	100mW/cm^2 white light source, 5mM PB, E = -0.15V vs Ag/AgCl	none	-13.7	ACS Appl. Mater. Interfaces, 2021, 13, 11237
FTO / mesoporous ITO / PSI	PSI from *T. elongatus*	100mW/cm^2 white light, 100mM MES (pH 6) + 400 mM KCl, E = -0.1V vs Ag/AgCl	none	-10.1	Biosensors and Bioelectronics, 2022, 214, 114495

ITO= Indium Tin oxide, DCPIP = 2,6-dichlorophenolindophenol, AscH = ascorbic acid, ATO = Antimony-doped Tin oxide, rGO = reduced Graphene Oxide, AMF = aminomethyl ferrocene, Q0 = ubiquinone-0, TMPD = N,N,N',N'-tetramethyl-p-phenylenediamine, DCBQ = 2, 6-dichloro-1,4-benzoquinone, PEI = polyethylenimine, SIF = silver island film, AgND = silver nano disk, p-Os = osmium polymer, PPy = polypyrrole film, PPA = poly(*p*-anisidine)

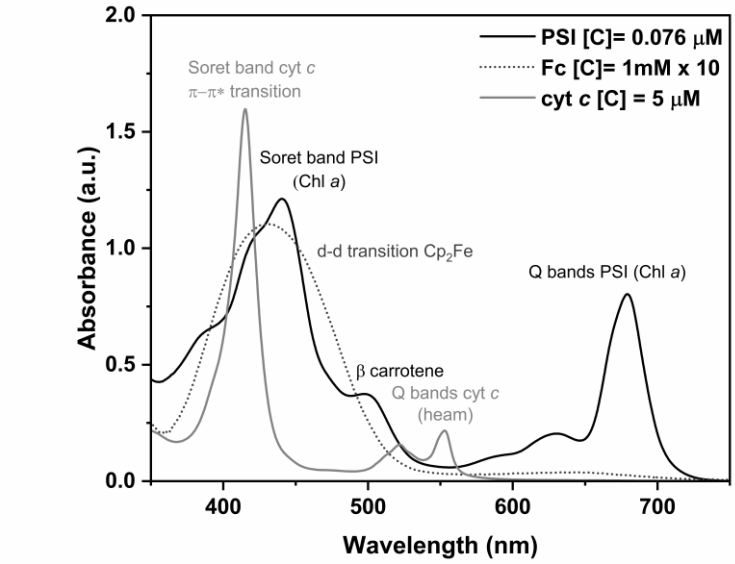

Fig. S10. UV-Vis spectra of ferrocene dimethanol (light dotted grey), His-tagged cytochrome c_{553} 19AA (grey), and PSI solution (dark). The PSI solution was composed of HEPES washing buffer solution [40 mM Hepes-NaOH / 3 mM CaCl / 25% (w/v) glycerol / 0.03% (w/w) DDM] diluted by 200 in H_2O. The His-tagged cyt c_{553} (19AA) solution was composed of 0.1 M PB with 25% glycerol (w/v) diluted 100-fold in H_2O. The 1 mM Fc solution was prepared in 0.1 M PB.

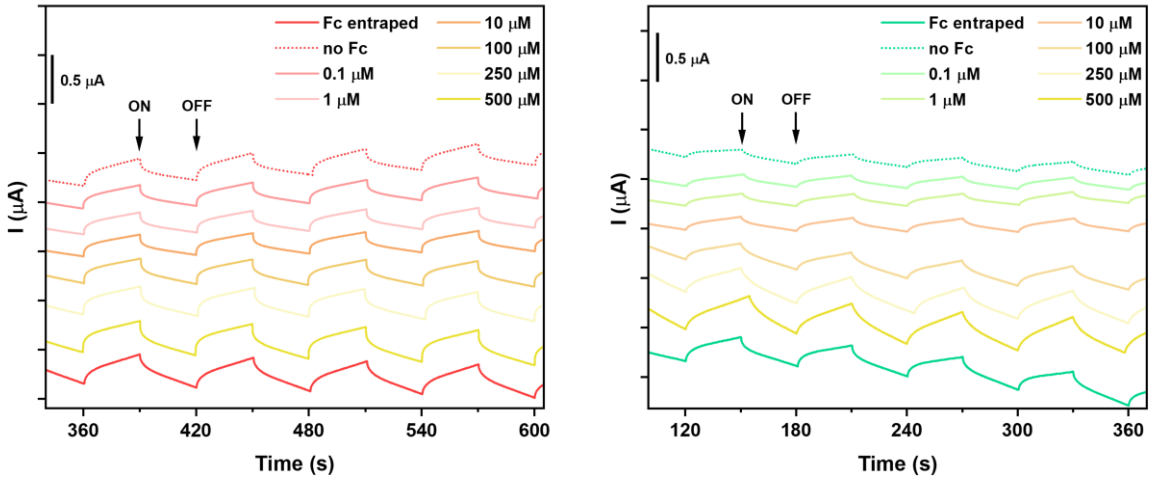

Fig. S11. Chopped photochronoamperometric curves recorded at -300 mV vs Ag/AgCl for (left) FTO-*c*NTA-Ni-cyt and (right) FTO-*c*NTA-Ni-cyt-PSI with entrapped Fc and without entrapped Fc in presence of increasing concentrations of diffusive Fc in 5 mM PB electrolyte (pH 7).

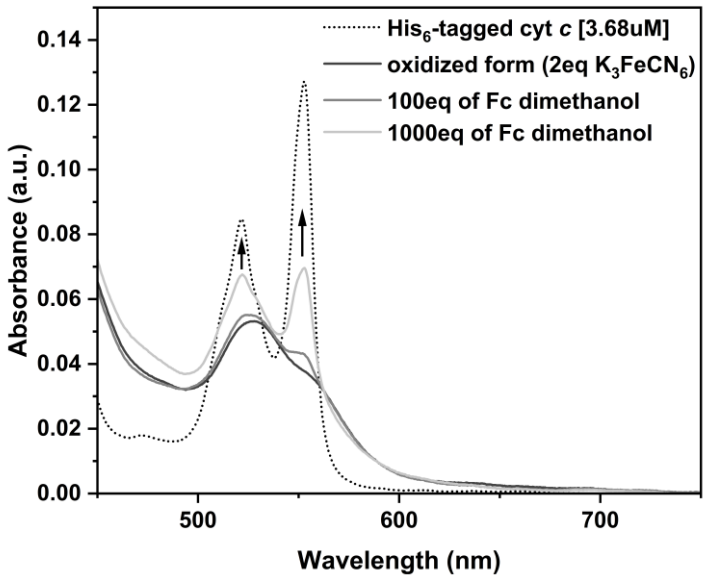

Fig. S12. UV-visible spectral changes of cyt *c* reduction by ferrocene dimethanol. The initial cyt *c* solution in 0.1 M phosphate buffer (PB) [C]=3.68 µM (dotted line) has been fully oxidized by the addition of 2 equivalents of K_3FeCN_6 solution in 0.1 M PB [C]=3.68 mM (dark grey line). The re-reduction of cyt *c* has been recorded following the addition of 100 (grey line) and 1000 equivalents (light grey line) of ferrocene dimethanol. For clarity, a baseline correction has been applied with the spectra of the respective equivalent solution devoid of cyt *c* that was recorded in parallel.

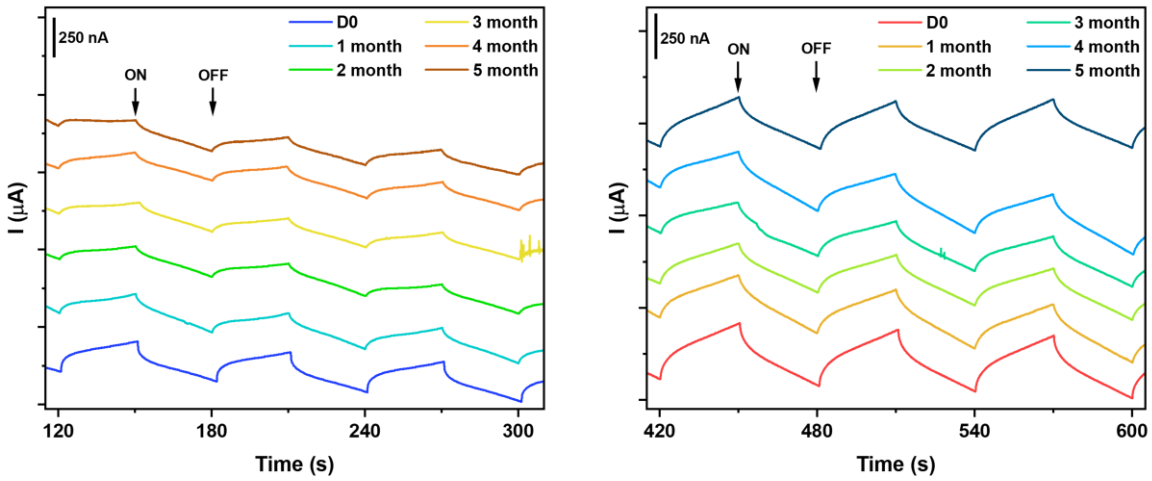

Fig. S13. Chopped photochronoamperometric curves recorded at -300 mV vs Ag/AgCl in 5 mM PB electrolyte (pH 7) for (left) FTO-*c*NTA-Ni and (right) FTO-*c*NTA-Ni-cyt with entrapped Fc over long-term storage. The electrodes were kept in oxygenated 5 mM PB solution in the dark at 4°C between each weekly photocurrent measurements in fresh 5 mM PB electrolyte.

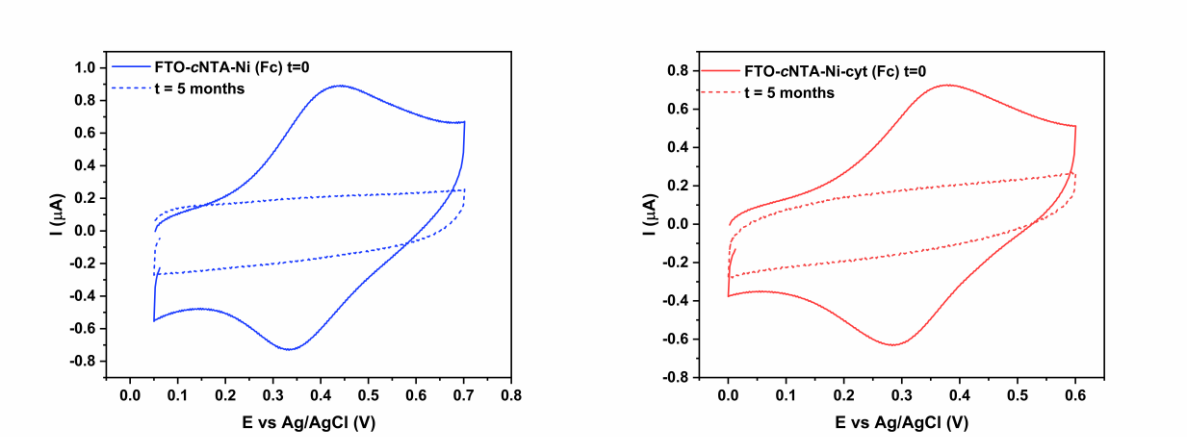

Fig. S14. Cyclic voltammograms of FTO-*c*TA-Ni and FTO-*c*NTA-Ni-cyt with entrapped Fc recorded at 50 mV s^{-1} in deoxygenated 5 mM PB solution for freshly prepared samples (full line) and after 5 months (dotted line). The electrodes were kept in oxygenated 5 mM PB solution in the dark at 4°C between each weekly photocurrent measurements in fresh 5 mM PB electrolyte during 5 months.

Table S6. Complementary parameters for the calculation of the cyt *c* surface coverage from the corrected Faradic current (Ip) and the area of the redox peaks (Π).

Scan rate (V/s)	Ip[Ox] (A)	Γ (mol/cm²)	Π [Ox] (A.V)	Γ (mol/cm²)	Ip[Red] (A)	Γ (mol/cm²)	Π [Red] (A.V)	Γ (mol/cm²)
0.002	5.39^{E-9}	7.46^{E-12}	7.7175^{E-10}	1.04^{E-11}	-7.57^{E-9}	1.05^{E-11}	1.109^{E-9}	1.49^{E-11}
0.004	7.69^{E-9}	5.32^{E-12}	1.1157^{E-9}	7.51^{E-12}	-9.82^{E-9}	6.79^{E-12}	1.544^{E-9}	1.04^{E-11}
0.006	1.05^{E-8}	4.85^{E-12}	1.7226^{E-9}	7.73^{E-12}	-1.18^{E-8}	5.42^{E-12}	1.9611^{E-9}	8.80^{E-12}
		5.88^{E-12}		8.55^{E-12}		7.57^{E-12}		11.37^{E-12}

Average value from the linear plot I=f(v): $\Gamma = 9.85 \cdot 10^{-12}$ mol/cm²
Average value from corrected Ip: $\Gamma = 6.73 \cdot 10^{-12}$ mol/cm²
Average value from Π: $\Gamma = 9.96 \cdot 10^{-12}$ mol/cm²

Table S7. Complementary parameters for the calculation of the space-confined Fc surface coverage from the corrected Faradic current (Ip) and the area of the redox peaks (Π).

Fc samples (at 0.025 V/s)	Ip[Ox] (A)	Γ (mol/cm²)	Π [Ox] (A.V)	Γ (mol/cm²)	Ip[Red] (A)	Γ (mol/cm²)	Π [Red] (A.V)	Γ (mol/cm²)
1	1.960^{E-7}	2.17^{E-11}	4.009^{E-8}	4.32^{E-11}	-1.918^{E-7}	2.12^{E-11}	4.460^{E-8}	4.81^{E-11}
2	3.172^{E-7}	3.51^{E-11}	6.991^{E-8}	7.53^{E-11}	-2.558^{E-7}	2.83^{E-11}	5.164^{E-8}	5.56^{E-11}
3	2.614^{E-7}	2.89^{E-11}	6.077^{E-8}	6.55^{E-11}	-2.234^{E-7}	2.47^{E-11}	4.670^{E-8}	5.03^{E-11}
Fc samples (at 0.05 V/s)	Ip[Ox] (A)	Γ (mol/cm²)	Π [Ox] (A.V)	Γ (mol/cm²)	Ip[Red] (A)	Γ (mol/cm²)	Π [Red] (A.V)	Γ (mol/cm²)
1	3.158^{E-7}	1.75^{E-11}	6.969^{E-8}	3.75^{E-11}	-3.166^{E-7}	1.75^{E-11}	7.510^{E-8}	4.05^{E-11}
2	5.966^{E-7}	3.30^{E-11}	1.368^{E-7}	7.37^{E-11}	-4.764^{E-7}	2.63^{E-11}	9.762^{E-8}	5.26^{E-11}
3	4.774^{E-7}	2.64^{E-11}	1.164^{E-7}	6.27^{E-11}	-4.08^{E-7}	2.26^{E-11}	8.299^{E-8}	4.47^{E-11}
Fc samples (at 0.1 V/s)	Ip[Ox] (A)	Γ (mol/cm²)	Π [Ox] (A.V)	Γ (mol/cm²)	Ip[Red] (A)	Γ (mol/cm²)	Π [Red] (A.V)	Γ (mol/cm²)
1	5.138^{E-7}	1.42^{E-11}	1.129^{E-7}	3.04^{E-11}	-5.789^{E-7}	1.60^{E-11}	1.582^{E-7}	4.26^{E-11}
2	1.041^{E-6}	2.88^{E-11}	2.476^{E-7}	6.67^{E-11}	-9.533^{E-7}	2.64^{E-11}	2.30^{E-7}	6.20^{E-11}
3	7.724^{E-7}	2.14^{E-11}	1.828^{E-7}	4.92^{E-11}	-8.055^{E-7}	2.23^{E-11}	1.805^{E-7}	4.86^{E-11}

Average		$2.52\pm0.5^{E-11}$		$5.60\pm1.28^{E-11}$		$2.28\pm0.31^{E-11}$		$4.94\pm0.48^{E-11}$

Average value from the linear plot I=f(v): $\Gamma = 2.36\pm0.4\cdot10^{-11}$ mol/cm^2
Average value from corrected Ip: $\Gamma = 2.40\pm0.4\cdot10^{-11}$ mol/cm^2
Average value from Π: $\Gamma = 5.27\pm0.88\cdot10^{-11}$ mol/cm^2

References.

1 B. Hirschorn, M. E. Orazem, B. Tribollet, V. Vivier, I. Frateur and M. Musiani, *Electrochim. Acta*, 2010, **55**, 6218–6227.

2 M. Jacquet, S. Osella, E. Harputlu, B. Pałys, M. Kaczmarek, E. K. Nawrocka, A. A. Rajkiewicz, M. Kalek, P. P. Michałowski, B. Trzaskowski, C. G. Unlu, W. Lisowski, M. Pisarek, K. Kazimierczuk, K. Ocakoglu, A. Więckowska and J. Kargul, *Chem. Mater.*, 2022, **34**, 3744–3758.